

Imaging Simulation Of A Dual-Panel PET Geometry With Ultrafast TOF Detectors

Taiyo Ishikawa, Go Akamatsu, Hideaki Tashima, Fumihiko Nishikido, Fumio Hashimoto, Ryosuke Ota, Hideaki Haneishi, Sun Il Kwon, Simon R. Cherry, and Taiga Yamaya

Abstract—In positron emission tomography (PET), time-of-flight (TOF) information localizes source positions along lines of response. Cherenkov-radiator-integrated microchannel-plate photomultiplier tubes have achieved 30 ps TOF resolution, demonstrating cross-sectional imaging without reconstruction. Such ultrafast TOF detectors would free PET from conventional ring geometries. Therefore, this study aimed at investigating imaging characteristics of a dual-panel PET with ultrafast TOF detectors using Geant4 simulation. Two detector panels ($142 \times 142 \text{ mm}^2$), which consisted of 5.0 mm-thick bismuth germanate pixelized crystals with a 5.75 mm pitch, were placed face-to-face at a 300 mm distance. Spatial resolution and image noise with various TOF resolutions from 30 to 90 ps were evaluated. Because degraded efficiency may cancel TOF gain in image quality, detection efficiency was also parameterized by reducing coincidence counts. A numerical phantom, which consisted of multi-rod and uniform cylindrical activities (21 MBq in total), was simulated for 600 s. Regarding image reconstruction, results of a backprojection (i.e., no reconstruction) were compared with those of the maximum likelihood expectation maximization (MLEM). The dual-panel PET required a 40 ps TOF resolution to have a similar spatial resolution to that of a non-TOF ring PET (300 mm in diameter) for the same detection efficiency. The TOF resolution should be 30 ps with half the efficiency to maintain a similar image noise to that of the 40 ps TOF with complete efficiency. MLEM provided better imaging performance than backprojection, even at 30 ps TOF. The feasibility of the proposed dual-panel PET with ultrafast TOF detectors was shown.

Index Terms— Positron emission tomography (PET), direct positron emission imaging, dual-panel PET, time-of-flight (TOF) PET, ultrafast timing resolution

I. INTRODUCTION

IN positron emission tomography (PET), time-of-flight (TOF) in the coincidence detection localizes the source position along a line of response (LOR) [1], [2]. Researchers have continued to improve TOF resolution [3] and it has reached around 200 ps, corresponding to 3 cm spatial resolution, in a state-of-the-art commercial clinical

This work did not involve human subjects or animals in its research.

Taiyo Ishikawa, Fumio Hashimoto, Hideaki Haneishi, and Taiga Yamaya are with Chiba University, Chiba 263-8522, Japan (e-mail: t_ishikawa@chiba-u.jp). Taiyo Ishikawa, Go Akamatsu, Hideaki Tashima, Fumihiko Nishikido, Fumio Hashimoto and Taiga Yamaya are with the National Institutes for Quantum Science and Technology (QST), Chiba 263-8555, Japan (e-mail: yamaya.taiga@qst.go.jp). Fumio Hashimoto and Ryosuke Ota are with Hamamatsu Photonics K.K., Hamamatsu 434-8601, Japan. Sun Il Kwon and Simon R. Cherry are with the University of California, Davis, Davis, CA 95616, USA

This work has been submitted to the IEEE for possible publication. Copyright may be transferred without notice, after which this version may no longer be accessible.

PET systems [4]. On a laboratory bench scale, a pair of Cherenkov-radiator-integrated microchannel plate photomultiplier tubes (CRI-MCP-PMT) has achieved a TOF resolution of ~30 ps [5]; the TOF resolution itself has become almost equal to the spatial resolution of clinical PET systems [6]. Kwon *et al.* [7] have demonstrated cross-sectional imaging by estimating the source point directly from TOF information obtained with a pair of detectors, without rotation and reconstruction. This ultrafast TOF resolution is expected to free PET from a conventional ring-shaped detector geometry, which is expected to open up new applications of PET.

Among such non-ring geometries, a dual-panel or partial ring geometry has been investigated for almost two decades [8], [9], [10], [11], [12], [13], [14]. A large open space around the patient is appropriate for PET-guided surgery [15], [16] and in-beam particle therapy monitoring [17]. In addition, a new concept named walk-through PET, which utilizes an imager with a standing position to realize high throughput and low patient burden, has also been proposed [18]. In addition, some organ-dedicated PET systems have been developed with the expectation of improved spatial resolution by placing detectors closer to each other [10], [19], [20]. In these systems, however, a limited projection view causes artifacts in the reconstruction [12]. TOF is expected to reduce these artifacts, but the currently available TOF resolution of around 200 ps is insufficient for this task [9].

It was demonstrated that 30 ps TOF resolution enabled cross-sectional imaging in the bench-top prototype [7]. However, the required TOF resolution and detection efficiency for the extension to a clinical system have yet to be properly investigated. Especially with respect to detection efficiency, detecting and triggering on Cherenkov photons is challenging because of their extremely small number compared to scintillation photons. The low detection efficiency may cancel the benefit of better TOF in terms of image noise. In addition, although the previous research claimed that reconstruction is unnecessary, the image quality of direct imaging has yet to be compared with that of iterative reconstruction.

This study focused on investigating the imaging characteristics of a dual-panel PET with ultrafast TOF resolution, in anticipation of the expansion of the setup of [7] to a human-sized clinical system. We quantitatively evaluated the spatial resolution and image noise to determine the required TOF resolution.

II. MATERIALS AND METHODS

A. Geometry

Fig. 1 shows the detector geometries of the proposed dual-panel and a ring PET. The ring PET was modeled as a reference for spatial resolution. The dual-panel PET had two detector panels (142 mm \times 142 mm) placed face-to-face at a 300 mm distance. The ring PET had five detector rings with a 300 mm diameter and 142 mm axial length.

The dual-panel PET was composed of 50 detectors, and the ring PET was composed of 160 detectors. The detectors were composed of 4×4 arrays of pixelized bismuth germanate (BGO) crystals, each sized as 5.75 \times 5.75 \times 5.0 mm³. This choice was based on multi-anode CRI-MCP-PMTs (5.75 mm readout pitch) [21] with a BGO window as a future possible extension of currently commercially available multi-anode MCP-PMTs (R10754-07-M16, Hamamatsu Photonics K. K.) [22].

B. Simulation

We modeled the dual-panel and ring geometries in the Geant4 Monte Carlo simulation [23]. We did not implement optical simulation this time. We assumed that Cherenkov photons provided detection timing information, and scintillation photons provided position and energy information in the dual-panel PET, based on the properties of BGO [24].

The decay process of a positron emitter was approximated by directly generating a positron without kinetic energy. Generated positrons were annihilated with electrons in the air. The effects of positron range and photon non-collinearity were neglected.

During the simulation, position, energy, and detection timing information were obtained for each energy deposition. In the case of multiple interactions in the detector, the crystal with the maximum energy deposition was treated as the detection position. Deposited energy was summed for each array, and energy resolution was applied using a Gaussian function with 20% full width at half maximum (FWHM) [25]. We used a 400 – 600 keV energy window.

The detection timing was calculated from the interaction time at the detection position and the distance between the

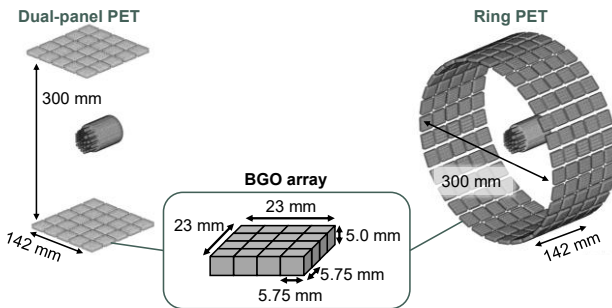


Fig. 1. Simulated geometries of the dual-panel PET and the ring PET. The detector had 4×4 array of BGO crystals, each sized 5.75 \times 5.75 \times 5.0 mm³. The dual-panel PET had 50 detectors (5 \times 5 detectors per panel), whereas the ring PET had 160 detectors (32 detectors per ring).

interaction position with the maximum energy deposition and the center of the crystal bottom surface. The photon travel time was added to the interaction time, based on the assumption that the detected first photon traveled linearly to the photocathode without reflection or scattering. For simplicity, the speed of light in the BGO crystals was calculated assuming a photon with wavelength 490 nm and a refractive index of 2.15 [26]. Coincidence detection information was recorded as list-mode data.

The TOF resolution was modeled with a Gaussian function. A random number generated from the Gaussian function was added to TOF information, which was the difference between the two detection timings of the list-mode data. In the Cherenkov/scintillation hybrid measurement with BGO crystals, the TOF resolution is well modeled by multiple Gaussian distributions with different FWHMs [27]. In this study, we assumed coincidence events in the dual-panel PET were triggered by Cherenkov photons, and those in the ring PET were triggered by scintillation photons for TOF resolution modeling.

Cherenkov photons produced via the interaction of annihilation radiation with the BGO crystals are highly variable and may not be detected [28]. We simulated the reduction in detection efficiency by randomly thinning out the list-mode data. The ratio of events remaining after thinning was defined as the relative detection efficiency (RDE). In other words, RDE was the hypothetical ratio of the Cherenkov-Cherenkov events among all the coincidences.

C. Numerical Phantom

We defined a numerical phantom composed of a multi-rod area and a uniform area to evaluate the spatial resolution and image noise in a single measurement (Fig. 2). The multi-rod area consisted of clusters of rods, 15 mm in height and 6, 5, 4, 3, 2.2, or 1.6 mm in diameter. The uniform area consisted of a cylinder, 50 mm in height and 45 mm in diameter. Only the radioactivity distribution was defined, and no attenuating material was simulated. We simulated 600-s of data acquisition for the phantom with 21 MBq activity.

D. Image Reconstruction

We used list-mode maximum likelihood expectation maximization (MLEM) and backprojection (i.e., no reconstruction) for image reconstruction. We used in-house code [29], and we implemented detector response function modeling with a TOF response function for projector and backprojectors in the MLEM. The detector response function in the direction perpendicular to the LOR was modeled as a Gaussian function [30] for the distance between each LOR and the center of each voxel with 2.5 mm FWHM. The TOF response function was modeled by convolving a rectangular function of TOF bin size with a Gaussian function having the FWHM of TOF resolution [31]. Let the l -axis be a line along a LOR. The center where a coincidence event is recorded is given by

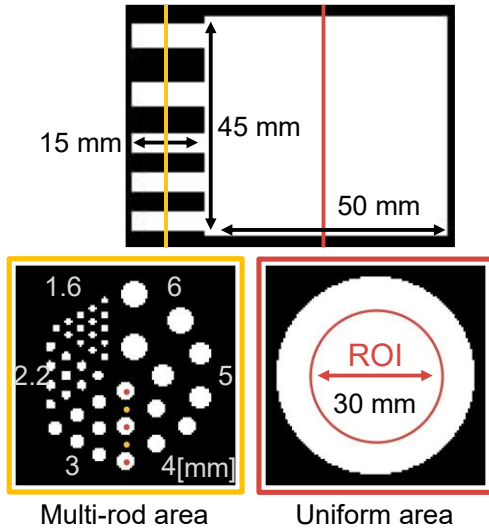


Fig. 2. Activity distribution of the numerical phantom. The phantom did not interact with annihilation radiation. The spatial resolution was evaluated through the percentage peak-to-valley ratio of 4-mm rods aligned perpendicular to the detector panels. The peak and valley positions are indicated by red and yellow dots, respectively, in the bottom left illustration. The image noise was evaluated by the percentage standard deviation of the region of interest (ROI) shown in the uniform area.

$$l_0 = \frac{ct}{2}, \quad (1)$$

where c is the speed of light, and t is the difference of arrival time. The probability density function along the LOR was given by

$$p(l) = \frac{1}{D} \text{rect}\left(\frac{1}{D}(l - l_0)\right) * \frac{1}{\sqrt{2\pi}\sigma} \exp\left\{-\frac{l^2}{2\sigma^2}\right\}, \quad (2)$$

where D is the TOF bin size, which was 1.2 mm, and $\sigma = \frac{\text{FWHM}}{2\sqrt{2\ln 2}}$ is the standard deviation. We should note that only the MLEM without TOF information was applied for the ring PET because we used it as a reference for the spatial resolution. The maximum number of MLEM iterations was 200. The voxel size of the reconstructed images was $1.0 \times 1.0 \times 1.0$ mm³.

A direct method was used for normalization. A hollow ring phantom was used for the ring PET. The hollow ring consisted of a positron distribution of 1 MBq, 2 mm in thickness, 288 mm in diameter, and 142 mm in axial length. The data acquisition time was 64800 s. For the dual-panel PET, a flat plate-shaped positron distribution of 1 MBq with a surface of 142×142 mm² and a thickness of 2 mm was set. The phantom was placed in the middle between the two detector panels and parallel to them. The data acquisition time was 21600 s.

We used the same backprojector as MLEM for backprojection. TOF response function modeling in backprojection will blur reconstructed images. A most-likely-point backprojector was also used to suppress the blurring. We assumed that the most likely point was l_0 in (1). To use the same backprojector as the TOF response function, the

rectangular function was convolved with a Gaussian function with 1.0 ps FWHM (0.15 mm spatial information). Dividing the backprojection image with a GSI, which was the backprojection of all the normalization factors, enabled the sensitivity correction.

E. Performance Evaluation

The image quality of the reconstructed images was evaluated for spatial resolution and image noise. Spatial resolution was evaluated from the resolution of the 4 mm diameter rods aligned perpendicular to the detector panels (Fig. 2). The percentage peak-to-valley ratio (%P2V), which represents the rod resolution, was defined as

$$\%P2V = (1 - avg_{v2p}) \cdot 100, \quad (3)$$

where avg_{v2p} is the average value of the four valley-to-peak ratios calculated for pairs of rod center points (peak) and midpoints (valley) adjacent to each other. The peak and valley positions are indicated by red and yellow dots, respectively, in the bottom left illustration in Fig. 2. Image noise was evaluated from the variation of pixel values in a circular region of interest (ROI). The circular ROI with a 30 mm diameter was set in a slice half the height of the cylindrical uniform area. Percentage standard deviation (%SD) was defined as

$$\%SD = \frac{std_{ROI}}{avg_{ROI}} \cdot 100, \quad (4)$$

where avg_{ROI} and std_{ROI} are the average and standard deviation of the pixel values in the circular ROI.

We investigated the imaging characteristics by varying the TOF resolution, RDE, and image reconstruction method.

1) Image quality for various TOF resolutions

We evaluated the image quality of the dual-panel PET with various TOF resolutions from 30 ps FWHM, which is the current best TOF resolution [5], to 90 ps FWHM. The data of the non-TOF ring PET were used as a reference for the spatial resolution. The image quality of the MLEM images changes depending on the number of iterations. Thus, we chose the number of iterations with the %SD closest to 10% for the spatial resolution study. For the image noise study, the %P2V was fixed at a value when %SD was 10% in the non-TOF ring PET.

2) Image quality for various RDEs

Reduced Cherenkov photon detection efficiency may cancel the TOF gain in image quality. Thus, we evaluated the image noise in the case of reduced detection efficiency. We varied RDE from 10% to 100% at 10% intervals because the valid event ratio where Cherenkov photons trigger both photosensors depends on the measurement setup [27], [32], [33]. In this comparison, we varied the TOF resolution as 30, 40, and 50 ps.

3) Backprojection vs. MLEM methods

To investigate the advantage of iterative reconstruction in ultrafast TOF resolution, we compared MLEM images with backprojection images. For this comparison, the TOF resolution was set to 30 ps. We used the backprojector of the TOF response function and most likely point for the backprojection.

III. RESULTS

A. Image quality for various TOF resolutions

Fig. 3 shows the %P2V-%SD curves in the MLEM iterations with 30, 40, 50, 60, and 90 ps TOF resolutions. The %P2V was increased with improving TOF resolution. The only exception was for the 40 ps TOF resolution at the %SD higher than 12.1%, where the %P2V was slightly higher than that of the 30 ps TOF resolution.

Fig. 4 shows the reconstructed images of the multi-rod area with 30, 40, 50, 60, and 90 ps TOF resolutions in the dual-panel PET and without TOF resolution in the ring PET. As the TOF resolution was improved, the artifacts in the vertical

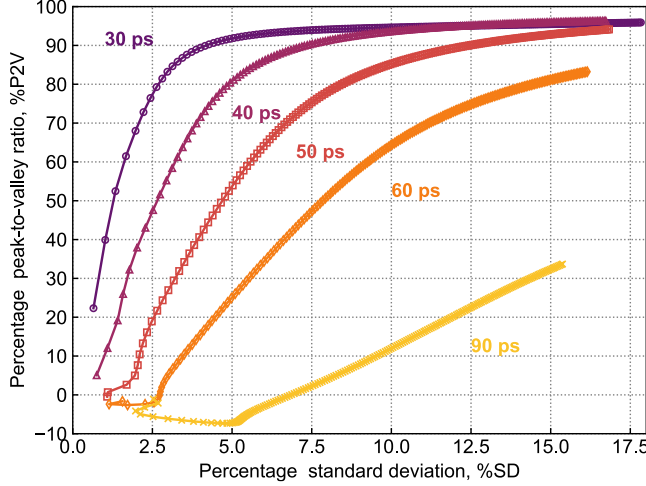


Fig. 3. The %P2V-%SD curves in the MLEM iterations with five TOF resolutions. Markers are plotted from one to 200 (left to right). %SD were decreased and %P2V were increased according to the TOF resolution.

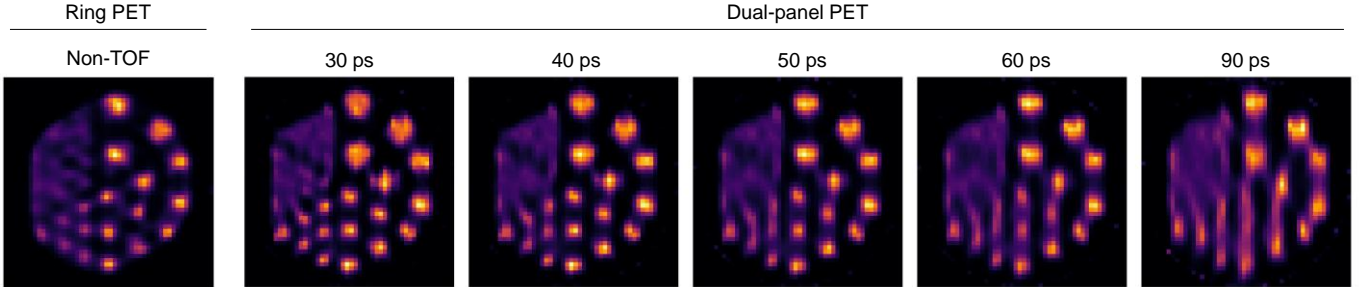


Fig. 4. MLEM images of the multi-rod area with various TOF resolutions from 30 ps to 90 ps. The MLEM image of the non-TOF ring PET is shown on the left. The iterations were selected at 10% of the %SD. As the TOF resolution was improved, the artifacts in the vertical direction were reduced in the dual-panel PET. The 3 mm rods were resolved with a better TOF resolution than 50 ps, which was the same rod resolution as that of the non-TOF ring PET.

direction were reduced. The 3 mm rods were resolved in the dual-panel PET images with better TOF resolutions than 50 ps, which was the same rod resolution as the non-TOF ring PET. The 4 mm rods were resolved even at 60 ps TOF resolution.

Fig. 5 shows the %P2V of the reconstructed images in Fig. 4. In the dual-panel PET, the %P2Vs at TOF resolutions of 30 ps (94.6%) and 40 ps (93.6%) were higher than in the non-TOF ring PET (92.3%). The average and standard deviation of %SD of the MLEM images were $10.0 \pm 0.03\%$.

Fig. 6 shows the uniform area of the reconstructed images. To compare the noise level at the same spatial resolution, the %P2V of these images was fixed at 92.3%, which was the value when the %SD was 10% in the non-TOF ring PET. As a result, the noise was reduced as the TOF resolution was improved. The %SD at 30, 40, and 50 ps TOF resolutions were 5.3%, 8.7%, and 14.4%, respectively.

B. Image quality for various RDEs

Fig. 7 shows the %SD for various RDEs. The MLEM iterations were selected when %P2V was higher than 91.3% and closest to 92.3%, which was when %SD was 10% in the non-TOF ring PET. The average and standard deviation of %P2V of the MLEM images were $92.3 \pm 0.1\%$. Even when reducing RDE to 50%, the %SD was comparable at 30 ps TOF resolution (8.3%) to that at 40 ps TOF resolution with complete efficiency (8.7%) (gray dashed line). However, the %SD at 30 ps TOF resolution with 30% RDE (10.3%) was worse than that at 40 ps TOF resolution with 80% RDE (8.9%). Similarly, the %SD at 30 ps TOF resolution with 20% RDE (15.8%) was worse than that at 50 ps TOF resolution with complete efficiency (14.4%).

C. Backprojection vs. MLEM methods

Fig. 8 shows the %P2V-%SD plot of the MLEM iterations and the backprojection images with the dual-panel PET at 30 ps TOF resolution. The backprojection image had a worse %SD but better %P2V with the most likely point than the TOF response function had. At the fixed %SD, the MLEM images exhibited higher %P2Vs than the backprojection images.

Fig. 9 shows the multi-rod area (top) and uniform area (bottom) of the reconstructed images plotted in Fig. 8. In terms of spatial resolution, the backprojection image obtained with the most likely point approach was more blurred than the MLEM image at the same %SD. In the backprojection images, the rods with diameter larger than 3 mm were resolved with the most likely point, whereas the rods with diameter larger than 4 mm were resolved with the TOF response function.

IV. DISCUSSION

In terms of the spatial resolution, 3 mm rods were resolved even at 50 ps TOF resolution in the proposed dual-panel PET (Fig. 4), and 40 ps TOF resolution was required to have a similar spatial resolution in the direction perpendicular to the detector panels as for the non-TOF ring PET (Fig. 5). The diameter of the ring PET and the panel-to-panel distance of

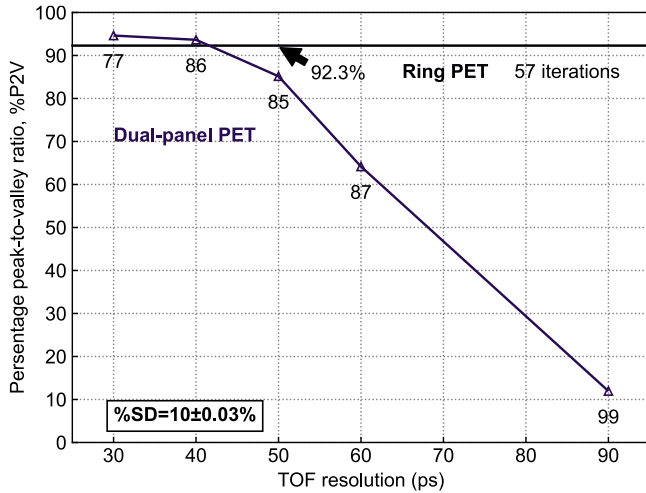


Fig. 5. Relation between %P2V and TOF resolution. The numbers of MLEM iterations are shown below each symbol for the dual-panel PET and below the line for the ring PET. The %P2V was higher at 30 ps TOF resolution (94.6%) and 40 ps TOF resolution (93.6%) in the dual-panel PET than the non-TOF ring PET (92.3%).

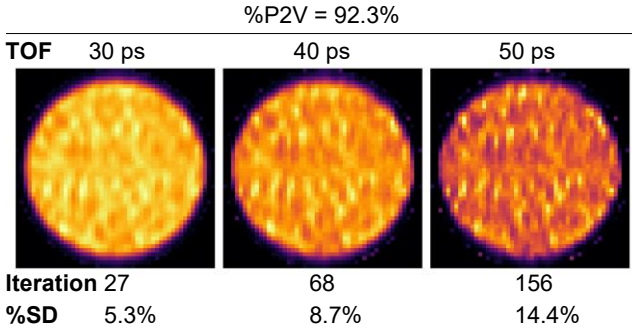


Fig. 6. MLEM images of the uniform area for TOF resolutions from 30 ps to 50 ps. The iterations were selected for a %P2V of 92.3% when %SD was 10% in the non-TOF ring PET. The image noise was decreased as the TOF resolution was improved.

the dual-panel PET were 300 mm in this comparison. The 300 mm diameter of the ring PET is insufficient for human whole-body imaging, and conventional whole-body PETs have larger diameters than 700 mm [4], [6]. The large ring diameter degrades the spatial resolution because of the photon non-

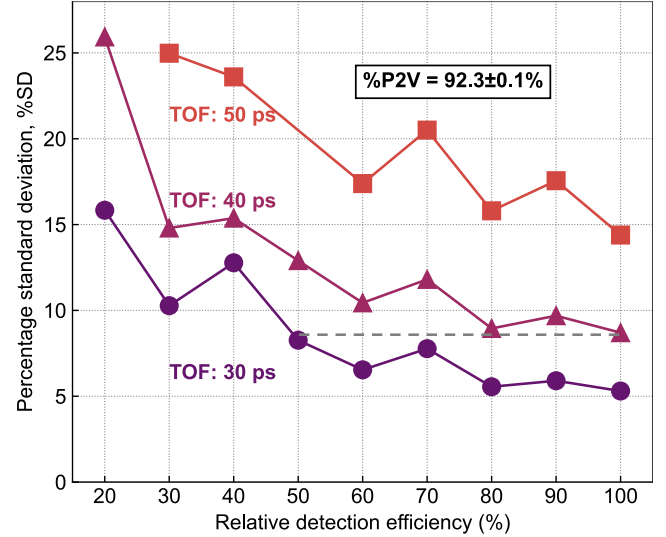


Fig. 7. Relation between RDE and %SD. The MLEM iterations were selected when %P2V was higher than 91.3% and closest to 92.3%, which was when %SD was 10% in the non-TOF ring PET. Even with RDE reduced to 50%, the %SD at TOF resolution of 30 ps (8.3%) was better than that at 40 ps with complete efficiency (8.7%) (gray dashed line). the %SD at 30 ps with 30% RDE (10.3%) was worse than that at 40 ps with 80% RDE (8.9%). The %SD at 30 ps with the 20% RDE (15.8%) was worse than that at 50 ps with complete efficiency (14.4%).

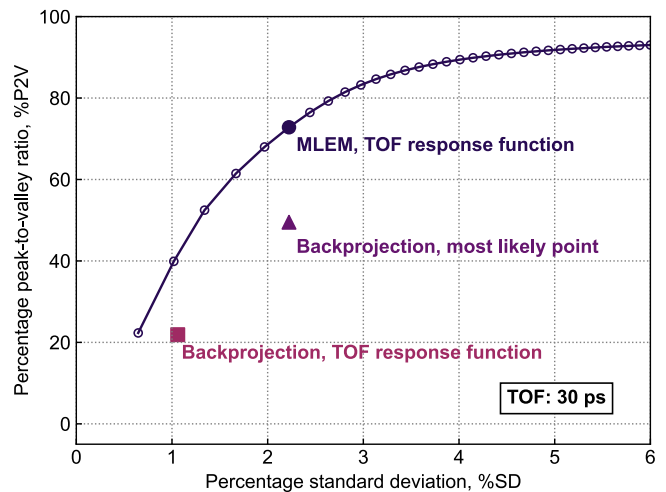


Fig. 8. The %P2V-%SD plot of MLEM iterations and backprojection images with the dual-panel PET at 30 ps TOF resolution. Markers are plotted from one to 33 (left to right) in MLEM plot. In the backprojection images, the most likely point had a worse %SD but better %P2V than the TOF response function. At a fixed %SD, the MLEM images showed higher %P2Vs than the backprojection images.

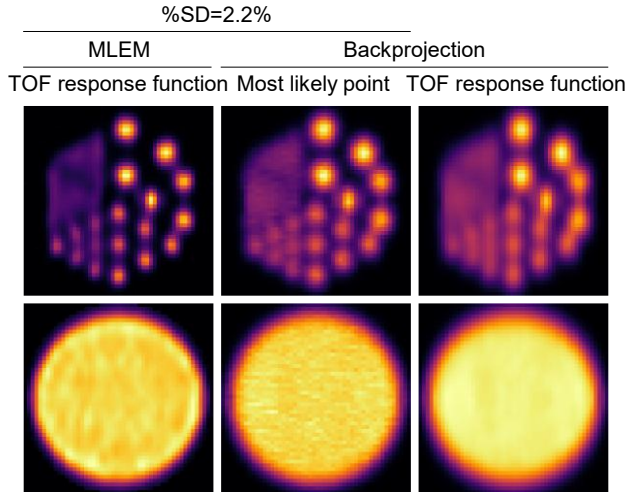


Fig. 9. Comparison of the reconstructed images between MLEM and backprojection with the dual-panel PET at 30 ps TOF resolution. The multi-rod areas and uniform areas were shown in the top row and bottom row, respectively. The MLEM image showed better spatial resolution than the backprojection image with the TOF response function at the same image noise level. In the backprojection images, the rods larger than 3 mm diameter were resolved with the most likely point, whereas the rods larger than 4 mm were resolved with the TOF response function.

colinearity. On the other hand, the dual-panel configuration can bring the detector panels close together. When the bottom detector panel was embedded in the patient's bed, we believe human whole-body imaging is possible with a 300 mm panel-to-panel distance. The required TOF resolution for the dual-panel PET in the present setup can be worse than 40 ps to have the same spatial resolution as the 800 mm-diameter ring PET. The rods 3 mm in diameter were resolved even with 40 ps TOF resolution, corresponding to 6.0 mm spatial resolution. This rod resolution was possible because the oblique LORs compensated for the spatial information in the direction perpendicular to the detector panels.

The image noise was reduced according to the TOF resolution when the same efficiency was maintained in the detectors (Fig. 6). In the case of reduced efficiency of the detectors (Fig. 7), image noise was comparable at 30 ps TOF resolution with half the efficiency and at 40 ps TOF resolution with complete efficiency. We showed that the TOF information could compensate for the loss of image quality due to reduced efficiency. The detection efficiency of the Cherenkov event is determined by multiple detector parameters, such as the stopping power of the BGO crystals, the number of the generated photons that reach the photocathode, and the event rate triggered by the Cherenkov photons [33]. We simplified these factors into one parameter, RDE. Further study is needed to investigate how these specific detector parameters change the detection efficiency.

The MLEM image showed better spatial resolution than the backprojection images did for the same noise level (Fig. 8, Fig. 9). This result showed that the iterative reconstructions

improved the image quality even with the ultrafast TOF resolution. It should be noted that MLEM requires many iterations and is computationally time-consuming; the present study reconfirmed these points.

In this study, we modeled the pixelized BGO crystals as the MCP-PMT window. However, it likely needs to be a monolithic crystal to maintain the vacuum inside the MCP-PMTs in realistic situations. Monolithic crystals will show better positional resolution than pixelized crystals having the same pitch as the anode pitch, because of the anger calculation [34]. On the other hand, the uniformity of the positional resolution will be degraded. TOF resolution will also vary [35]. These factors should be considered in future work.

The TOF-PET detector with BGO crystals shows a long tail in the timing histogram [36]. This tail is due to the variance of the number of the detected Cherenkov photons or the contamination of events triggered by only the scintillation photons. Several research groups are developing methods to identify whether single events are triggered by the Cherenkov photons or scintillation photons [27], [32], [33], [36], [37]. In this study, we assumed that this identification could be done correctly. The impact of identification failures on image quality needs to be investigated in the future.

Razdevšek *et al.* [14] investigated the imaging performance of a similar dual-panel system using Monte Carlo simulation. They used lutetium oxyorthosilicate crystals as scintillators. On the other hand, we used BGO crystals for the hybrid detection of Cherenkov and scintillation photons, which was the major difference between this study and the previous study.

As a reference scanner for the spatial resolution, we used BGO crystals as scintillators of 5 mm thickness for the non-TOF ring PET. However, Lu-based scintillators with 20 mm thickness are used for a commercial scanner having 214 ps TOF resolution [4]. In addition to the TOF information, the higher stopping power contributes to better image noise levels than the results obtained in this study. We need to investigate the required specifications for the dual-panel PET to outperform the Lu-based ring PET in a further study.

V. CONCLUSION

We investigated imaging characteristics of the dual-panel PET with ultrafast TOF resolution using Geant4 simulation. The TOF resolution required for the dual-panel PET to have a similar spatial resolution performance to that of the non-TOF ring PET was determined to be 40 ps for the same efficiency in the detectors. In the case of half the efficiency, we showed that the TOF resolution should be 30 ps to maintain a similar level of image noise to that of the 40 ps TOF resolution with complete efficiency. The MLEM images showed better spatial resolution than the backprojection images at the same noise level, even at 30 ps TOF resolution. In conclusion, our simulation results supported the feasibility of the proposed dual-panel PET with the ultrafast TOF detector.

ACKNOWLEDGMENT

All authors declare that they have no known conflicts of interest in terms of competing financial interests or personal relationships that could have an influence or are relevant to the work reported in this paper.

This work was partially supported by the Japan Society for the Promotion of Science (JSPS) KAKENHI Grant Number 20H05667 and the Nakatani Foundation.

REFERENCES

[1] T. Tomitani, “Image reconstruction and noise evaluation in photon time-of-flight assisted positron emission tomography,” *IEEE Trans. Nucl. Sci.*, vol. 28, no. 6, pp. 4581–4589, Feb. 1981, doi: 10.1109/TNS.1981.4335769.

[2] D. L. Snyder, L. J. Thomas, and M. M. Ter-Pogossian, “A mathematical model for positron-emission tomography systems having time-of-flight measurements,” *IEEE Trans. Nucl. Sci.*, vol. 28, no. 3, pp. 3575–3583, Jun. 1981, doi: 10.1109/TNS.1981.4332168.

[3] S. Vandenberghe, E. Mikhaylova, E. D’Hoe, P. Mollet, and J. S. Karp, “Recent developments in time-of-flight PET,” *EJNMMI Phys.*, vol. 3, no. 1, p. 3, Dec. 2016, doi: 10.1186/s40658-016-0138-3.

[4] J. van Sluis *et al.*, “Performance characteristics of the digital Biograph Vision PET/CT system,” *J. Nucl. Med.*, vol. 60, no. 7, pp. 1031–1036, Jul. 2019, doi: 10.2967/jnumed.118.215418.

[5] R. Ota *et al.*, “Coincidence time resolution of 30 ps FWHM using a pair of Cherenkov-radiator-integrated MCP-PMTs,” *Phys. Med. Biol.*, vol. 64, no. 7, p. 07LT01, Mar. 2019, doi: 10.1088/1361-6560/ab0fce.

[6] A. Chicheportiche, R. Marciano, and M. Orevi, “Comparison of NEMA characterizations for Discovery MI and Discovery MI-DR TOF PET/CT systems at different sites and with other commercial PET/CT systems,” *EJNMMI Phys.*, vol. 7, no. 1, p. 4, Jan. 2020, doi: 10.1186/s40658-020-0271-x.

[7] S. I. Kwon *et al.*, “Ultrafast timing enables reconstruction-free positron emission imaging,” *Nat. Photonics*, vol. 15, no. 12, pp. 914–918, Dec. 2021, doi: 10.1038/s41566-021-00871-2.

[8] E. Lee, M. E. Werner, J. S. Karp, and S. Surti, “Design optimization of a time-of-flight, breast PET scanner,” *IEEE Trans. Nucl. Sci.*, vol. 60, no. 3, pp. 1645–1652, Jun. 2013, doi: 10.1109/TNS.2013.2257849.

[9] S. Surti and J. S. Karp, “Design considerations for a limited angle, dedicated breast, TOF PET scanner,” *Phys. Med. Biol.*, vol. 53, no. 11, p. 2911, May 2008, doi: 10.1088/0031-9155/53/11/010.

[10] A. S. Manesh, M. Amini, H. Arabi, K. Doroud, C. Williams, and H. Zaidi, “Conceptual design of a dual-panel dedicated prostate PET scanner: a Monte Carlo simulation study,” in *2022 IEEE Nuclear Science Symposium and Medical Imaging Conference (NSS/MIC)*, Jan. 2022, pp. 1–3, doi: 10.1109/NSS/MIC44845.2022.10399251.

[11] J. Zhang, P. D. Olcott, G. Chinn, A. M. K. Foudray, and C. S. Levin, “Study of the performance of a novel resolution dual-panel PET camera design dedicated to breast cancer imaging using Monte Carlo simulation,” *Med. Phys.*, vol. 34, no. 2, pp. 689–702, 2007, doi: 10.1118/1.2409480.

[12] P. Crespo, G. Shakirin, and W. Enghardt, “On the detector arrangement for in-beam PET for hadron therapy monitoring,” *Phys. Med. Biol.*, vol. 51, no. 9, p. 2143, Apr. 2006, doi: 10.1088/0031-9155/51/9/002.

[13] A. Gonzalez-Montoro *et al.*, “Design and proof of concept of a double-panel TOF-PET system,” *EJNMMI Phys.*, vol. 11, no. 1, p. 73, Aug. 2024, doi: 10.1186/s40658-024-00674-8.

[14] G. Razdevsek *et al.*, “Multipanel limited angle PET system with 50 ps FWHM coincidence time resolution: a simulation study,” *IEEE Trans. Radiat. Plasma Med. Sci.*, vol. 6, no. 6, pp. 721–730, Jul. 2022, doi: 10.1109/TRPMS.2021.3115704.

[15] S. Sajedi, L. Bläckberg, S. Majewski, and H. Sabet, “Limited-angle TOF-PET for intraoperative surgical applications: proof of concept and first experimental data,” *J. Instrum.*, vol. 17, no. 01, p. T01002, Jan. 2022, doi: 10.1088/1748-0221/17/01/T01002.

[16] B. Li *et al.*, “A panel PET with window: design, performance evaluation, and prototype development,” *IEEE Trans. Radiat. Plasma Med. Sci.*, vol. 1, no. 4, pp. 310–321, Jul. 2017, doi: 10.1109/TRPMS.2017.2706284.

[17] V. Ferrero *et al.*, “Online proton therapy monitoring: clinical test of a Silicon-photodetector-based in-beam PET,” *Sci. Rep.*, vol. 8, no. 1, p. 4100, Mar. 2018, doi: 10.1038/s41598-018-22325-6.

[18] S. Vandenberghe *et al.*, “Walk-through flat panel total-body PET: a patient-centered design for high throughput imaging at lower cost using DOI-capable high-resolution monolithic detectors,” *Eur. J. Nucl. Med. Mol. Imaging*, vol. 50, no. 12, pp. 3558–3571, Oct. 2023, doi: 10.1007/s00259-023-06341-x.

[19] M. Li, B. Yockey, and S. Abbaszadeh, “Design study of a dedicated head and neck cancer PET system,” *IEEE Trans. Radiat. Plasma Med. Sci.*, vol. 4, no. 4, pp. 489–497, Jul. 2020, doi: 10.1109/TRPMS.2020.2964293.

[20] A. J. González, F. Sánchez, and J. M. Benlloch, “Organ-dedicated molecular imaging systems,” *IEEE Trans. Radiat. Plasma Med. Sci.*, vol. 2, no. 5, pp. 388–403, Sep. 2018, doi: 10.1109/TRPMS.2018.2846745.

[21] L. Ma *et al.*, “A novel multi-anode MCP-PMT with Cherenkov radiator window,” *Nucl. Instrum. Methods Phys. Res. Sect. Accel. Spectrometers Detect. Assoc. Equip.*, vol. 1049, p. 168089, Apr. 2023, doi: 10.1016/j.nima.2023.168089.

[22] “Microchannel plate photomultiplier tube R10754-07-M16 | Hamamatsu Photonics.” Accessed: Jun. 30, 2024. [Online]. Available: <https://www.hamamatsu.com/jp/en/product/optical->

sensors/pmt/pmt_tube-alone/mcp-pmt/R10754-07-M16.html

[23] J. Allison *et al.*, “Geant4 developments and applications,” *IEEE Trans. Nucl. Sci.*, vol. 53, no. 1, pp. 270–278, Feb. 2006, doi: 10.1109/TNS.2006.869826.

[24] S. E. Brunner and D. R. Schaart, “BGO as a hybrid scintillator / Cherenkov radiator for cost-effective time-of-flight PET,” *Phys. Med. Biol.*, vol. 62, no. 11, p. 4421, May 2017, doi: 10.1088/1361-6560/aa6a49.

[25] H. Zhang *et al.*, “Performance characteristics of BGO detectors for a low cost preclinical PET scanner,” *IEEE Trans. Nucl. Sci.*, vol. 57, no. 3, pp. 1038–1044, Jun. 2010, doi: 10.1109/TNS.2010.2046753.

[26] G. E. Jellison, Jr., S. Auluck, D. J. Singh, and L. A. Boatner, “Optical properties of bismuth germanate,” *J. Appl. Phys.*, vol. 107, no. 1, p. 013514, Jan. 2010, doi: doi:10.1063/1.3272909.

[27] N. Kratochwil, E. Auffray, and S. Gundacker, “Exploring cherenkov emission of BGO for TOF-PET,” *IEEE Trans. Radiat. Plasma Med. Sci.*, vol. 5, no. 5, pp. 619–629, Sep. 2021, doi: 10.1109/TRPMS.2020.3030483.

[28] S. Gundacker *et al.*, “Experimental time resolution limits of modern SiPMs and TOF-PET detectors exploring different scintillators and Cherenkov emission,” *Phys. Med. Biol.*, vol. 65, no. 2, p. 025001, Jan. 2020, doi: 10.1088/1361-6560/ab63b4.

[29] S. Takyu *et al.*, “Design study of a brain-dedicated time-of-flight PET system with a hemispherical detector arrangement,” *Phys. Med. Biol.*, vol. 65, no. 3, p. 035012, Feb. 2020, doi: 10.1088/1361-6560/ab63ee.

[30] J. Cui, G. Pratx, S. Prevrhal, and C. S. Levin, “Fully 3D list-mode time-of-flight PET image reconstruction on GPUs using CUDA,” *Med. Phys.*, vol. 38, no. 12, pp. 6775–6786, 2011, doi: 10.1118/1.3661998.

[31] T. Yamaya, T. Obi, M. Yamaguchi, and N. Ohyama, “High-resolution image reconstruction method for time-of-flight positron emission tomography,” *Phys. Med. Biol.*, vol. 45, no. 11, p. 3125, Jan. 2000, doi: 10.1088/0031-9155/45/11/301.

[32] S. I. Kwon, E. Roncali, A. Gola, G. Paternoster, C. Piemonte, and S. R. Cherry, “Dual-ended readout of bismuth germanate to improve timing resolution in time-of-flight PET,” *Phys. Med. Biol.*, vol. 64, no. 10, p. 105007, May 2019, doi: 10.1088/1361-6560/ab18da.

[33] A. Gonzalez-Montoro, S. Pourashraf, J. W. Cates, and C. S. Levin, “Cherenkov radiation-based coincidence time resolution measurements in BGO scintillators,” *Front. Phys.*, vol. 10, Jan. 2022, doi: 10.3389/fphy.2022.816384.

[34] A. González-Montoro, F. Sánchez, P. Bruyndonckx, G. Cañizares, J. M. Benlloch, and A. J. González, “Novel method to measure the intrinsic spatial resolution in PET detectors based on monolithic crystals,” *Nucl. Instrum. Methods Phys. Res. Sect. Accel. Spectrometers Detect. Assoc. Equip.*, vol. 920, pp. 58–67, Mar. 2019, doi: 10.1016/j.nima.2018.12.056.

[35] W.-S. Choong, “Investigation of a multi-anode microchannel plate PMT for time-of-flight PET,” *IEEE Trans. Nucl. Sci.*, vol. 57, no. 5, pp. 2417–2423, Oct. 2010, doi: 10.1109/TNS.2010.2060211.

[36] N. Kratochwil, S. Gundacker, P. Lecoq, and E. Auffray, “Pushing Cherenkov PET with BGO via coincidence time resolution classification and correction,” *Phys. Med. Biol.*, vol. 65, no. 11, p. 115004, Jun. 2020, doi: 10.1088/1361-6560/ab87f9.

[37] R. Ota and K. Ote, “Emphasizing Cherenkov photons from bismuth germanate by single photon response deconvolution,” *IEEE Trans. Radiat. Plasma Med. Sci.*, vol. 8, no. 6, pp. 595–606, Jul. 2024, doi: 10.1109/TRPMS.2024.3403959.